crystals

MDPI

Article

Nanocrystallization of the Cu$_{46}$Zr$_{33.5}$Hf$_{13.5}$Al$_7$ Metallic Glass

Jaskaran S. Saini [1,2,3] †, Tamara D. Koledin [1,2,] †, Tittaya Thaiyanurak [1,2], Lei Chen [1,2], Melissa K. Santala [1,2], Donghua Xu [1,2,]*

[1] Materials Science Program, Oregon State University, Corvallis, OR 97331, U.S.A.
[2] School of Mechanical, Industrial and Manufacturing Engineering, Oregon State University, Corvallis, OR 97331, U.S.A.
[3] Department of Nanoengineering, University of California, San Diego, CA 92037, U.S.A.

† These authors contributed equally to this work.
* Correspondence: Donghua.Xu@oregonstate.edu

Abstract: The recently discovered Cu$_{46}$Zr$_{33.5}$Hf$_{13.5}$Al$_7$ (at.%) bulk metallic glass (BMG) presents the highest glass-forming ability (GFA) among all known copper-based alloys, with a record-breaking critical casting thickness (or diameter) of 28.5 mm [J.S. Saini, C. Palian, F.Q. Lei, A. Dyall, N. AuYeung, R. McQuade, S.K. Gupta, D.P. Cann, D.H. Xu, Applied Physics Letters 116, 011901 (2020)]. At present, much remains to be explored about this new BMG which holds exceptional promise for engineering applications. Here, we report our study on the crystallization behavior of this new BMG, using isochronal and isothermal differential scanning calorimetry (DSC), X-ray diffraction (XRD), and transmission electron microscopy (TEM). With the calorimetric data, we determine the apparent activation energy of crystallization, the Avrami exponent, and the lower branch of the isothermal time-temperature-transformation (TTT) diagram. With XRD and TEM, we identify primary and secondary crystal phases utilizing samples crystallized to different degrees within the calorimeter. We also estimate the number density, nucleation rate and growth rate of the primary crystals through TEM image analysis. Our results reveal that the crystallization in this BMG has a high activation energy of ≈360 kJ/mole, and that the primary crystallization of this BMG produces a high number density (≈10^{21} m^{-3} at 475 °C) of slowly growing (growth rate <0.5 nm/s at 475 °C) Cu$_{10}$(Zr,Hf)$_7$ nanocrystals dispersed in the glassy matrix, while the second crystallization event further produces a new phase Cu(Zr,Hf)$_2$. The results help understand the GFA and thermal stability of this new BMG and provide important guidance for its future engineering applications, including its usage as a precursor to glass-crystal composite or bulk nanocrystalline structures.

Keywords: metallic glass; crystallization; nucleation and growth; Cu alloys; nano-crystal; amorphous alloys; ImageJ; supercooled liquid; calorimetry

Citation: To be added by editorial staff during production.

Academic Editor: Firstname Lastname

Received: date
Revised: date
Accepted: date
Published: date

1. Introduction

Bulk metallic glasses (BMGs) are a new generation of metallic materials that are dramatically different from conventional engineering metals or alloys [1-5]. They possess an overall disordered structure, without any crystal grains or crystal-related defects (e.g., grain boundaries, dislocations) which widely exist in the conventional metals or alloys. Because of this, BMGs exhibit a host of properties far exceeding their crystalline counterparts, such as strength, hardness, wear and corrosion-resistance, elastic strain limit, resilience, and magnetic softness (for ferromagnetic BMGs) [1-5]. In addition, they bring out new manufacturing opportunities for metal industry, for example, thermoplastic processing far below the melting temperature, near net-shape casting, microstructure control by partial or full crystallization of the amorphous matrix [6,7].

Nevertheless, a number of challenges remain to be solved before the advantages of BMGs can be widely utilized in industry. Among these is their still limited glass-forming ability (GFA). When a BMG is manufactured (usually by melt casting), its smallest dimension, which dominates the heat transfer, must be kept below a threshold value, in order to obtain fast enough cooling and freeze the melt directly into a disordered (glassy) structure. This threshold is termed the critical casting thickness (or, diameter for a cylindrical rod), L_c. The L_c is a manifestation of the GFA, and correspondingly, the manufacturability of a BMG. Unfortunately, most BMGs discovered to date possess a critical casting thickness below 15 mm [8-17], which significantly limits their possible engineering applications. This is a common problem across many different types of BMGs, including copper (Cu) based BMGs which are of broad interest due to the attractive characteristics of copper (e.g., low cost, abundant supply, high ductility, high electrical and thermal conductivity).

Recently, a new series of Cu-based BMGs, $Cu_{46}Zr_{47-x}Hf_xAl_7$ ($8 \le x \le 20$ at.%) have been discovered at Oregon State University which possess exceptional GFA with the critical casting thickness exceeding 15 mm [14]. In particular, $Cu_{46}Zr_{33.5}Hf_{13.5}Al_7$ possesses a critical casting thickness at least 28.5 mm, marking a new record for any Cu-based BMG alloy. Furthermore, unlike the few earlier reported BMGs with similar (or better) GFA, e.g., Zr-Ti-Cu-Ni-Be, Pd-Cu-Ni-P, Mg-Cu-Ag-Gd, La-Al-Cu-Ag-Ni-Co [8], these new Cu-Zr-Hf-Al BMGs are free of toxic elements (e.g., Be), precious metals (e.g., Pd, Ag) and rare earths (e.g., Gd, La), which makes them even more attractive for engineering applications. At present, much remains to be explored about these new Cu-Zr-Hf-Al BMGs, for example, the origin of GFA, thermal stability, atomic structure (chemical and topological short-range ordering), mechanical properties (elastic and plastic deformation mechanisms), and electrical properties.

Here, we focus on the crystallization behavior of the $Cu_{46}Zr_{33.5}Hf_{13.5}Al_7$ BMG which has the highest GFA among all Cu-based BMGs. Studying crystallization behavior may help understand the GFA and thermal stability and guide future engineering applications of this exceptional BMG, including its usage as a precursor to glass-crystal composite and bulk nano-crystalline structures. We perform isochronal (constant heating-rate) and isothermal differential scanning calorimetry (DSC) experiments on as-cast samples to determine the apparent activation energy of crystallization, the Avrami exponent, and the lower branch of the isothermal time-temperature-transformation (TTT) diagram. We also perform X-ray diffraction (XRD) and transmission electron microscopy (TEM) on samples crystallized to different degrees within the calorimeter, to identify the primary and secondary crystal phases, and estimate the number density and the nucleation and growth rates of the primary crystals. We discuss our results in connection with the GFA, thermal stability, and potential applications of the $Cu_{46}Zr_{33.5}Hf_{13.5}Al_7$ BMG.

2. Experimental Methods

An alloy ingot of the $Cu_{46}Zr_{33.5}Hf_{13.5}Al_7$ BMG is produced by arc melting (after ultrasonic cleaning) Cu (oxygen-free shots), Zr (crystal bar), Hf (crystal bar), and Al pieces having purities of 99.99%, 99.9+%, 99.2+%, and 99.99%, respectively, on a water-cooled copper stage that is tiltable from outside the arc melting chamber. Prior to the melting, the chamber is pumped to high vacuum with a residual pressure of 3×10^{-4} mbar, and then filled with ultrahigh purity argon. The atmosphere is then further purified by first melting a Zr-getter (placed at a separate position) before melting the Cu, Zr, Hf, and Al pieces. The $Cu_{46}Zr_{33.5}Hf_{13.5}Al_7$ alloy ingot is flipped and remelted eight times in the arc melter in order to obtain complete chemical homogeneity. The alloy ingot is then melted once again and tilt cast into a copper mold placed below the melting stage that has a 10 mm diameter cylindrical cavity. Small specimens are then cut from the cast rod using a high-speed diamond saw and used for DSC, XRD and TEM experiments.

A Mettler Toledo DSC 3 with platinum pans and flowing ultrahigh purity nitrogen is used for thermal analysis and for preparing XRD and TEM specimens with controlled degrees of crystallization. A range of heating rates from 2.5 to 40 K/min are employed for isochronal DSC. For isothermal DSC, the specimens are heated at a relatively high heating rate of 60 K/min to a target temperature and held there until completion of crystallization. A set of holding temperatures ranging from 470 to 500 °C are utilized for the isothermal DSC. In order to characterize the primary crystallization phase using XRD and TEM, an additional specimen is isothermally held at 475 °C inside the calorimeter just past the first exothermic peak and then quickly (≈150 K/min) cooled back to room temperature.

This partially crystallized specimen, an as-cast, and a fully crystallized (also at 475 °C) specimen are studied using XRD and TEM. For XRD, a Rigaku Smartlab X-ray diffractometer is used with a Cu-Kα source in a reflection (Bragg-Brentano) mode with θ-θ scan.

Specimens are prepared for TEM by cutting the materials into 3 mm diameter disks, thinning them to ≈40 μm, and polishing one side to a mirror finish with diamond paste. The second side is dimpled and polished with diamond paste, reducing the thickness to ≈15 μm. Specimens are then ion milled to perforation with argon at 5 keV, followed by 10 min at 2 keV. These accelerating voltages are carefully chosen to prevent ion-milling-induced phase transformations [18]. An FEI Titan TEM/STEM operated at 200 keV is used to take bright-field images of the microstructure and perform selected area electron diffraction (SAED).

3. Results and Discussion

3.1. Isochronal DSC

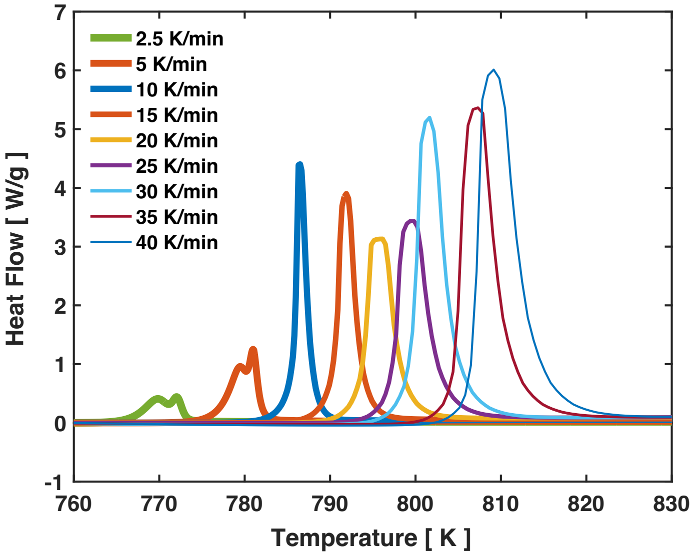

Figure 1. Crystallization signals (exothermic) recorded in isochronal DSC scans of as-cast specimens at nine different heating rates.

Figure 1 shows the exothermic DSC signals caused by crystallization during continuous isochronal heating at rates of 2.5, 5, 10, 15, 20, 25, 30, 35, and 40 K/min. As the heating rate increases, the DSC peak shifts to higher temperatures, which is as expected (due to less time spent at each temperature). At the two lowest heating rates, i.e., 2.5 and 5 K/min, the DSC peak displays two minor splittings that are close to each other, indicating that the crystallization proceeds with two steps: primary and secondary crystallization events. At the other (higher) heating rates, no peak splittings are apparent, most likely due to the overlap between the two steps at the higher crystallization temperatures. Indeed, increasing overlap between the two crystallization events at a higher heating rate is recognizable if one compares the DSC signals for the 2.5 and 5 K/min heating rates.

Kissinger's method is often used to analyze the correspondence between the DSC peak shift and the heating rate to extract an overall activation energy of a thermally activated process (e.g., chemical reaction or phase transformation) [19-21]. This method is based on the first-order chemical reaction model, and more specifically, the following equation:

$$\frac{dx}{dt} = Aexp\left(-\frac{E_a}{RT}\right)(1-x) \tag{1}$$

in which x is the dimensionless reacted (or transformed) fraction. This equation assumes that the reaction rate, dx/dt, is proportional to the remaining unreacted fraction $1-x$, and that the proportionality coefficient, or, the reaction rate constant, is solely determined by the temperature, T, according to the Arrhenius formulation which contains an activation energy, E_a, the universal gas constant, R, and a pre-exponential factor, A.

Based on Eq. (1) and the fact that the heat flow measured by DSC is essentially dx/dt (scaled by the total enthalpy of crystallization, i.e., the total area enclosed by the DSC peak), a relationship between the peak position (temperature), T_p, on the DSC signal, where the dx/dt is at its maximum, and the heating rate β employed in an isochronal scan can be theoretically derived by taking the derivative of Eq. (1) on both sides (note that T varies linearly with t as $dT/dt = \beta$) and setting that to zero. The result is the well-known Kissinger's equation:

$$\ln\left(\frac{\beta}{T_p^2}\right) = -\frac{E_a}{R}\frac{1}{T_p} + \ln A - \ln\frac{E_a}{R} \tag{2}$$

which suggests a linear correlation between $\ln\left(\frac{\beta}{T_p^2}\right)$ and $\frac{1}{T_p}$ with a slope equal to $-\frac{E_a}{R}$. Once the slope is known, the activation energy E_a can be conveniently determined.

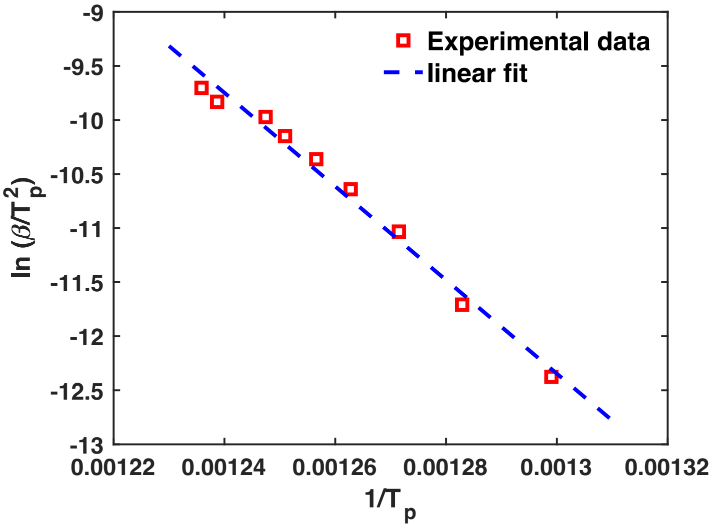

Figure 2. Kissinger plot based on the crystallization peaks in the isochronal DSC scans of as-cast specimens.

Figure 2 presents the so-called Kissinger plot of $\ln\left(\frac{\beta}{T_p^2}\right)$ vs. $\frac{1}{T_p}$ showing both experimental data and the fitted linear correlation. The Kissinger's model captures the experimental data quite well, with a fitting goodness (R^2) of 0.986. Using the slope from the linear fitting, the activation energy E_a for the crystallization is determined to be 360 kJ/mole.

In Figure 2, the data points representing the two lowest heating rates (2.5 and 5 K/min) are based on the first peak-splitting of the DSC signal as shown in Figure 1. If the second peak-splitting is used for these two heating rates (while data remain the same for the other heating rates), the Kissinger fitting is still reasonably good, albeit with a slightly lower R^2 of 0.977, and the activation energy E_a is determined to be 380 kJ/mole, even higher than the 360 kJ/mole reported above.

The values of E_a obtained here are larger than those reported for most other Cu-based metallic glasses in the literatures, for example, 208 kJ/mole for $Cu_{73}Sn_6Ni_6P_{15}$ [22], 331 kJ/mole for $Cu_{50}Zr_{40}Ti_{10}$ [23], 354 kJ/mole for $Cu_{43}Zr_{43}Al_7Ag_7$ [24]. A high activation energy for crystallization is generally in line with a high GFA because glass formation requires avoidance of crystallization (although glass is made most commonly through a cooling instead of heating process). Hence, the results here contribute to our understanding of the origin of the superior GFA of the $Cu_{46}Zr_{33.5}Hf_{13.5}Al_7$ BMG. From another perspective, a high activation energy for crystallization widens the temperature window for controlling the crystallization process so as to produce preferred microstructural characteristics (e.g., crystallite number density, grain size, remaining glass fraction) in the devitrified glass.

Note that Eq. (1), i.e., the first order chemical reaction model with a reaction rate constant solely decided by the temperature, as assumed in the Kissinger's method, is not strictly valid for phase transformations such as crystallization. A simple piece of evidence is that at a fixed temperature (and varying time), Eq. (1) predicts an exponential decay of DSC signal, which is not the case as to be seen in the next section of this paper or in the vast literature on isothermal DSC studies. Indeed, the Kolmogorov-Johnson-Mehl-Avrami (KJMA) model combined with appropriate descriptions for crystal nucleation and growth rates, which in whole is equivalent to Eq. (1) but with a time-dependent (power law) rate constant, is more applicable to phase transformations. Nonetheless, the Kissinger analysis does provide an overall activation energy that largely represents how difficult it is for crystallization to occur and that can be conveniently compared across different materials.

3.2. Isothermal DSC

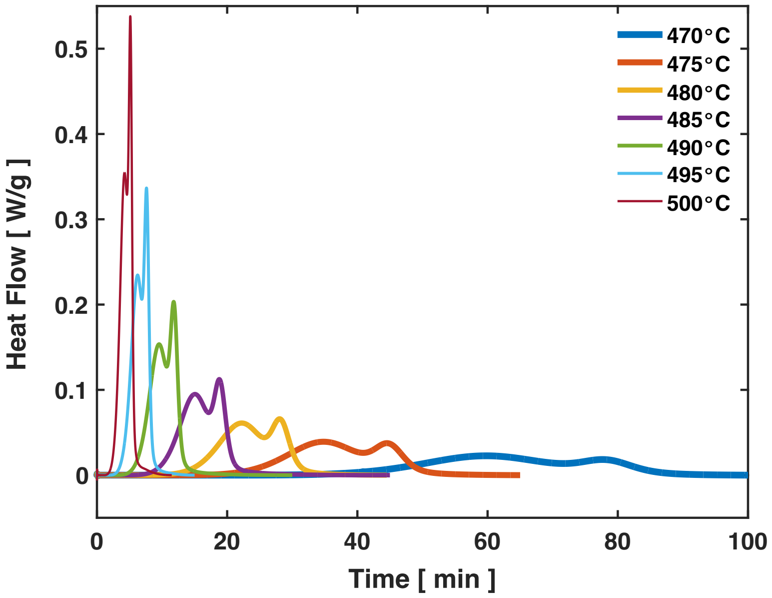

Figure 3. Crystallization signals (exothermic) recorded in isothermal DSC scans of as-cast specimens at seven different temperatures.

Figure 3 shows the isothermal DSC scans (heat flow vs. time) of the $Cu_{46}Zr_{33.5}Hf_{13.5}Al_7$ BMG obtained at seven different temperatures ranging from 470 to 500 °C. These temperatures are all above the apparent glass transition temperature, 454 °C, observed during the preheating (60 K/min) prior to the isothermal holding. All the isothermal scans display two crystallization events (peaks) and the two events become more and more overlapped with increasing temperature. These are consistent with observations in the isochronal DSC scans (especially those at 2.5 and 5 K/min heating rates).

The basic form of the KJMA model for phase transformations is:

$$dx = dx_{ext}(1 - x) \tag{3}$$

where x is the actual transformed fraction, and x_{ext} is the extended transformed fraction. The x_{ext} is a fictive quantity theoretically determined by integrating nucleation and growth rates over time without considering any spatial overlap of nuclei/grains or the continuous decrease of the remaining parental phase that limits later transformation. Generally, the extended fraction is expressed as $x_{ext} = \lambda t^m$, where t is the time, m is the so-called Avrami exponent and λ is a rate constant which comprises contributions from both nucleation and growth rates. Combining Eq. (3) and the power law of the x_{ext}, one can find $x = 1 - \exp(-\lambda t^m)$, and its differential form:

$$\frac{dx}{dt} = \lambda m t^{m-1} \exp(-\lambda t^m) \tag{4}$$

which is a single-event KJMA model for isothermal DSC signal (after baseline removal and normalization). Eq. (4) assumes that nucleation and growth of the new phase start from time zero. When there is an incubation period t_i, as often encountered, Eq. (4) can be modified to:

$$\frac{dx}{dt} = \lambda m (t - t_i)^{m-1} \exp[-\lambda (t - t_i)^m] \tag{5}$$

Since there are two crystallization events here, a two-event version of the KJMA model,

$$\frac{dx}{dt} = f_1 \lambda_1 m_1 (t - t_{i1})^{m_1 - 1} \exp[-\lambda_1 (t - t_{i1})^{m_1}]$$

$$+(1 - f_1)\, \lambda_2 m_2 (t - t_{i2})^{m_2 - 1} \exp[-\lambda_2 (t - t_{i2})^{m_2}] \tag{6}$$

is used to fit the isothermal DSC data in this study, where f_1 is the total fraction of transformation contributed by the first event. Care needs to be taken to properly implement this fitting. For example, to avoid imaginary numbers and associated numerical problems, the $t - t_{i1}$ and $t - t_{i2}$ should be compared with zero and replaced by zero, if negative, by the fitting program.

The two-event KJMA model fits the data very closely, with $R^2 > 0.99$ achieved for all seven temperatures. Examples of the fitted curves (the normalization factor, i.e., the total enthalpy of crystallization, reapplied for plotting) vs. experimental data are presented in Figure 4 with T = 475, 485, and 495 °C. The fitting results for the seven different temperatures are tabulated in Table 1. The fitted Avrami exponents (m_1, m_2) and incubation times (t_{i1}, t_{i2}) of the primary and the secondary crystallization events are plotted in Figure 5. As seen in Table 1 and Figure 5, the incubation time decreases with increasing temperature for both events. At 470 °C (16 °C above the glass transition temperature), the incubation time is rather long, 23.4 min for the primary event, and 68.2 min for the secondary event. At 500 °C, it becomes significantly shorter, 0.5 min and 4.6 min for the primary and secondary events, respectively.

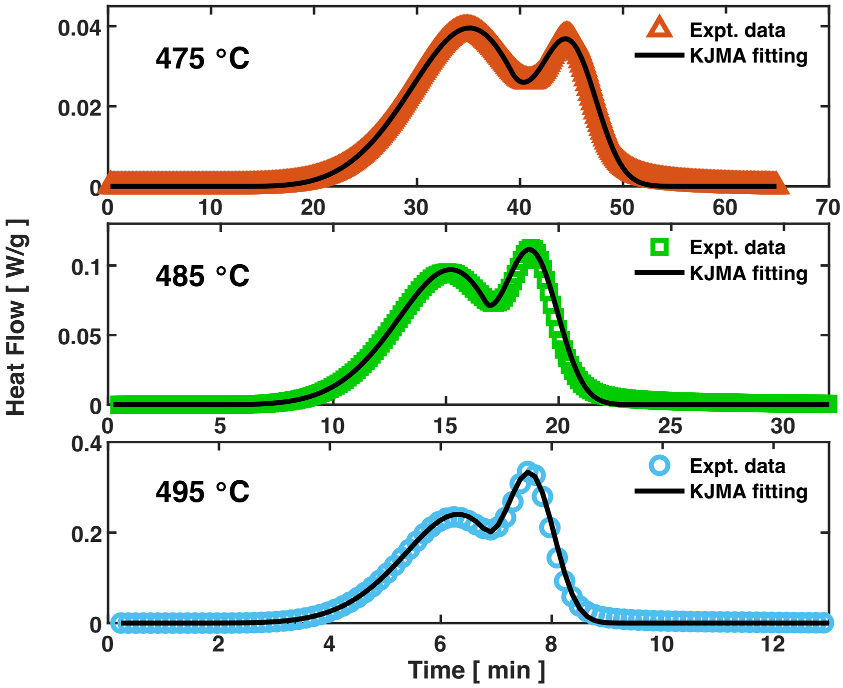

Figure 4. Examples of two-event KJMA model fitting of the isothermal DSC data.

Table 1. Two-event KJMA fitting results at seven temperatures.

T	f_1	λ_1	m_1	t_{i1} (min)	λ_2	m_2	t_{i2} (min)
470 °C	0.77	1.1×10^{-7}	4.37	23.43	8.7×10^{-4}	2.84	68.17
475 °C	0.73	1.8×10^{-7}	4.86	11.74	5.1×10^{-3}	2.78	39.26
480 °C	0.71	1.6×10^{-7}	5.50	5.80	0.020	2.77	24.82
485 °C	0.69	5.5×10^{-7}	5.77	3.45	0.086	2.55	16.80
490 °C	0.68	4.4×10^{-6}	5.97	1.97	0.24	2.75	10.46
495 °C	0.68	2.1×10^{-5}	6.35	0.99	0.92	2.76	6.80
500 °C	0.68	1.8×10^{-4}	6.39	0.53	2.70	2.63	4.60

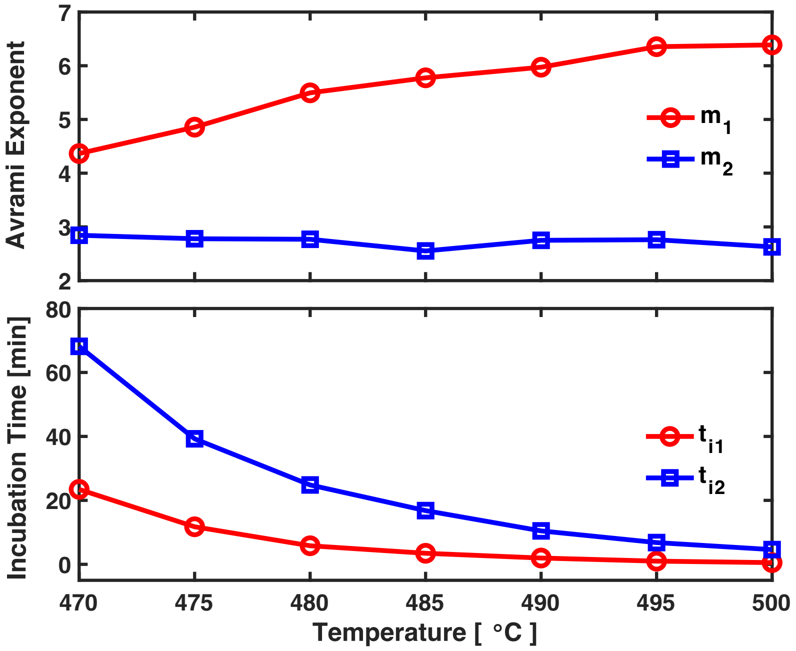

Figure 5. Fitted Avrami exponents (m) and incubation times (t_i) of the primary (subscript 1, i.e., m_1, t_{i1}) and the secondary (subscript 2, i.e., m_2, t_{i2}) crystallization events plotted as a function of temperature.

The Avrami exponent increases from 4.4 at 470 °C to 6.4 at 500 °C for the primary crystallization, while it stays fairly stable around 2.6 to 2.8 for the secondary crystallization. In the standard theory, the Avrami exponent is expected to range from 0.5 (instantaneous/heterogeneous nucleation and 1-D diffusion-controlled growth) to 4 (homogeneous nucleation and 3-D interface-controlled growth). More specifically, if the nucleation is homogeneous, the Avrami exponent is expected to take values of 2, 3, and 4 for 1-D, 2-D, and 3-D interface-controlled growth, and 1.5, 2, and 2.5 for 1-D, 2-D, and 3-D diffusion-controlled growth, respectively. If the nucleation is instantaneous/heterogeneous, these expected values all decrease by one. Apparently, the Avrami exponents obtained here do not fit into any of the standard cases.

The rising trend and the values of the Avrami exponent obtained here for the primary crystallization can be understood as the result from an increasing degree of non-steadiness of homogeneous nucleation that is hinted by the diminishing incubation time. At 470 °C, the incubation time is very long and the supercooled liquid matrix adjusts its topological and chemical short-range ordering (which is well known to exist in metallic glasses and their supercooled liquids [25-30]) and prepares for homogeneous nucleation in an approximately steady manner. The nearly steady-state homogeneous nucleation combined with 3-D interface-controlled growth (the 3-D dimensionality of the primary crystals can be seen from the TEM images in Section 3.4) results in an Avrami exponent of 4.4, only slightly above the standard value of 4. At higher holding temperatures, the incubation time becomes notably shorter and the local structural and chemical adjustment of the supercooled liquid matrix and the homogeneous nucleation of the primary crystal phase become increasingly non-steady, i.e., more dependent on time. This additional dependence on time is then manifested by the increase in the Avrami exponent.

The stability and the values of the Avrami exponent obtained here for the secondary crystallization can be understood as resulting from heterogeneous nucleation and a sub-3-D growth mode. It is conceivable that the primary crystals formed in the first crystallization event provide heterogeneous nucleation sites for the secondary crystallization, and in the meantime reduce (to below 3-D) the effective dimensionality of crystal growth in the second event as these secondary crystals grow from the surfaces of the primary crystals towards the remaining supercooled liquid matrix. This results in the fairly stable Avrami exponent around 2.6 - 2.8 for the secondary crystallization, which is slightly below the standard value of 3 for heterogeneous nucleation combined with 3-D growth mode.

From the isothermal DSC data presented in Figure 3, one can calculate the cumulative transformation curves (using numerical integration) which are displayed in Figure 6. Due to the existence of two crystallization events, the cumulative transformation curves all show a kink, although it is less noticeable at higher holding temperatures due to increased overlap between the primary and the secondary crystallization events (see Figure 3).

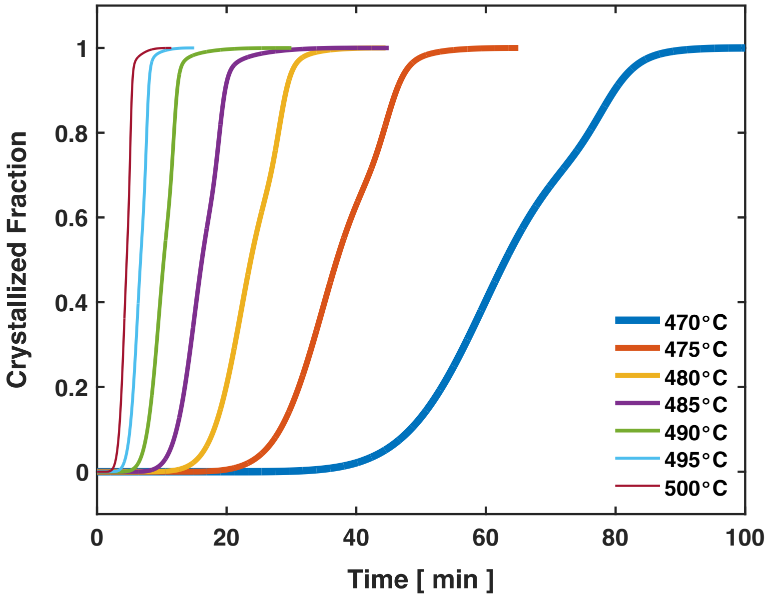

Figure 6. Cumulative transformation curves derived from the isothermal DSC scans at seven different temperatures.

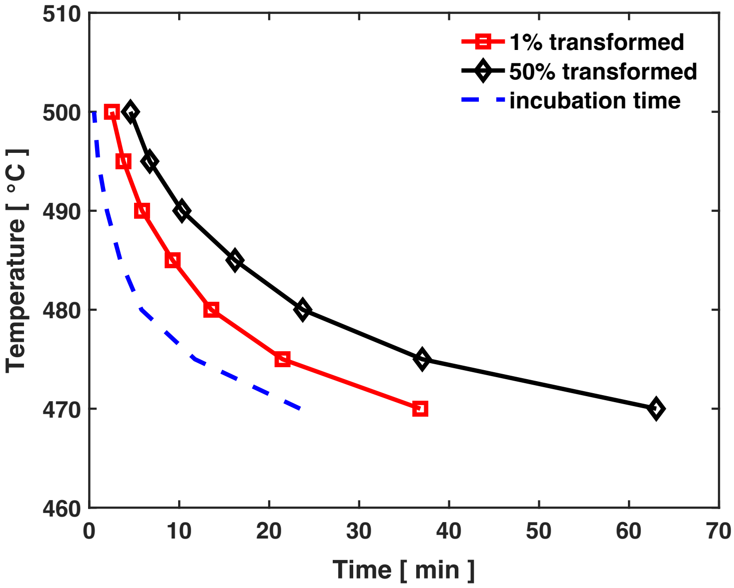

Figure 7. Time-temperature-transformation (TTT) diagrams derived from the cumulative transformation curves.

The cumulative transformation curves can be used to extract the time it takes to reach certain transformed fractions at varied temperatures and construct isothermal TTT diagrams. Figure 7 exhibits two TTT diagrams obtained here for the $Cu_{46}Zr_{33.5}Hf_{13.5}Al_7$ BMG, one representing a transformed fraction of 1% and the other 50%, together with the incubation time (for the first crystallization event) as a reference. A complete TTT diagram would exhibit a "C"-shape, with long transformation times in both high temperature (upper branch) and low temperature (lower branch, determined here) regimes. The upper branches of the TTT diagrams are not determined here, since isothermal holding in that temperature regime would require a very high heating rate (typically available on a flash DSC), or, fully melting the sample followed by rapid cooling to reach those target temperatures, which is beyond the capability of our instrument. Nonetheless, the lower branches of the TTT diagrams obtained here carry particular significance for informing the thermoplastic processing and controlled devitrification of the BMG and predicting the thermal stability of the BMG in applications at moderately elevated temperatures.

3.3. X-ray diffraction (XRD)

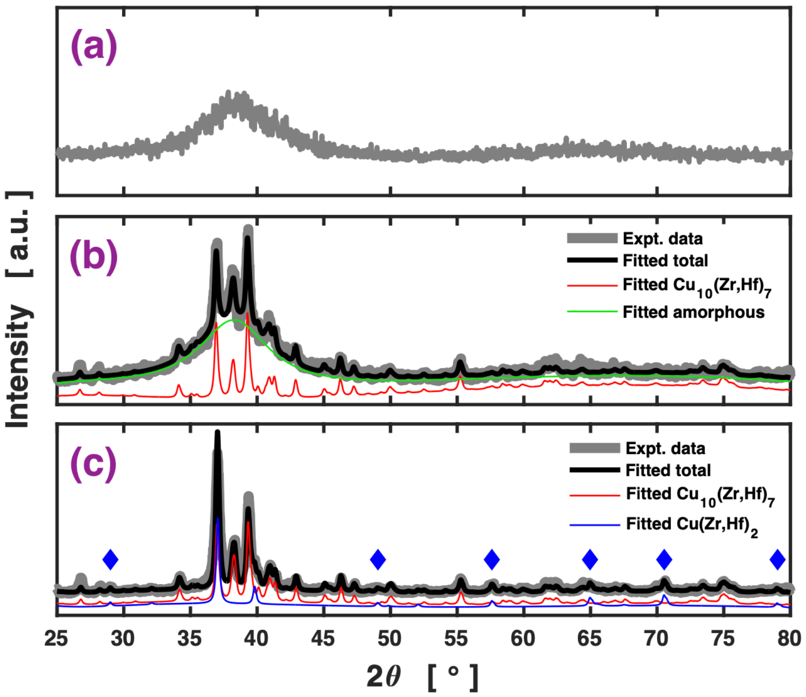

Figure 8. X-ray diffraction patterns of the as-cast specimen (a), the specimen annealed at 475 °C for 34 min (b), and the specimen annealed at 475 °C for 65 min (c). For the latter two specimens, fitted total and individual components using Rietveld refinement are also presented. The fitted individual components have been shifted in y-direction for clarity.

Figure 8a shows the XRD pattern of the as-cast specimen of the $Cu_{46}Zr_{33.5}Hf_{13.5}Al_7$ BMG. It consists of only diffuse/broad maxima (two in the scanned 25 to 80° range of 2θ), without any sharp Bragg peaks. This demonstrates the fully amorphous (glassy) structure of the as-cast specimen.

In Figure 8b, the thick gray line is the XRD pattern obtained from the specimen isothermally annealed inside the calorimeter at 475 °C for 34 min. This annealing time corresponds to the DSC peak of the primary crystallization event at this temperature (see Figure 3), and is shorter than the incubation time for the secondary crystallization event (see Table 1). Thus, only the primary crystal phase is expected to exist in this specimen. The open-source software Profex [31] is used to fit the XRD pattern through Rietveld refinement. As shown in Figure 8b, this XRD pattern is fitted very nicely with an amorphous phase and a single crystal phase: $Cu_{10}(Zr,Hf)_7$. The binary compounds $Cu_{10}Zr_7$ and $Cu_{10}Hf_7$ share the same structure (space group 64, Cmce, orthorhombic lattice) and similar lattice parameters [32,33], and hence both Zr and Hf are considered to be present in the primary crystal phase. The strong amorphous signal which is directly visible in the experimental data and further confirmed by the fitting suggests that the primary crystals co-exist with a substantial amount of remaining glass matrix, i.e., that the specimen has a glass-crystal composite structure.

The thick gray line in Figure 8c is the XRD pattern obtained from the specimen isothermally annealed inside the calorimeter at 475 °C for 65 min. According to the isothermal DSC data, this annealing time is longer than it takes for both primary and secondary crystallization events to complete at this temperature (see Figure 3). Thus, this specimen is expected to be fully crystallized and comprise both the primary and secondary crystal phases. Indeed, the XRD pattern exhibits no appreciable amorphous component, confirming that the specimen is fully crystallized. The Rietveld refinement finds a few new peaks (positions marked with the blue diamonds) that cannot be reproduced using the primary phase $Cu_{10}(Zr,Hf)_7$. These new peaks are found to agree with the $Cu(Zr,Hf)_2$ phase (space group 139, I4/mmm, tetragonal lattice). By considering both $Cu_{10}(Zr,Hf)_7$ and $Cu(Zr,Hf)_2$ phases, the whole XRD pattern is well fitted. The fitting also suggests that the secondary phase $Cu(Zr,Hf)_2$ has contributed to the main diffraction peaks near 37° and 39.3° in addition to the marked new peaks.

3.4. Transmission electron microscopy (TEM)

Figure 9 presents the bright-field images and overall SAED patterns of the same three specimens as in Section 3.3: the as-cast (a), the one annealed at 475 °C for 34 min (b), and the one annealed at 475 °C for 65 min (c). The TEM image of the as-cast specimen is smooth and featureless (note that the contrast at the lower left corner is due to thickness variation), typical of amorphous materials. The diffraction pattern consisting of two diffuse rings further confirms the amorphous structure of the specimen. This is also consistent with the XRD result presented in Figure 8a.

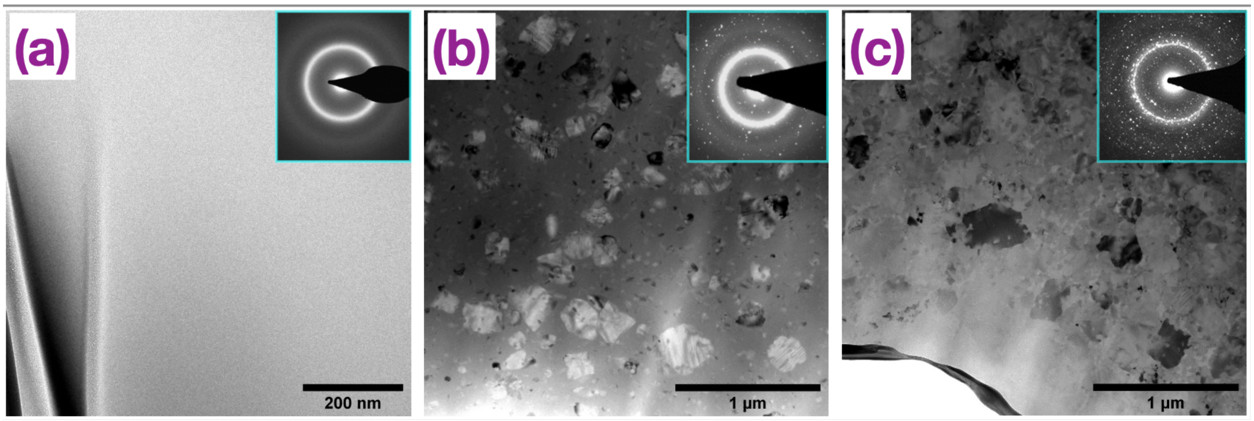

Figure 9. TEM bright-field images and SAED patterns (inset) of the as-cast specimen (a), the specimen annealed at 475 °C for 34 min (b), and the specimen annealed at 475 °C for 65 min (c).

The TEM image of the specimen annealed at 475 °C for 34 min in Figure 9b exhibits nearly equiaxed crystals of various sizes embedded in a featureless matrix. The corresponding overall SAED pattern is comprised of both diffuse amorphous rings and discrete spots from crystal grains. Both the image and the diffraction pattern confirm the glass-crystal composite structure of this partially crystallized specimen, consistent with the XRD data in Figure 8b.

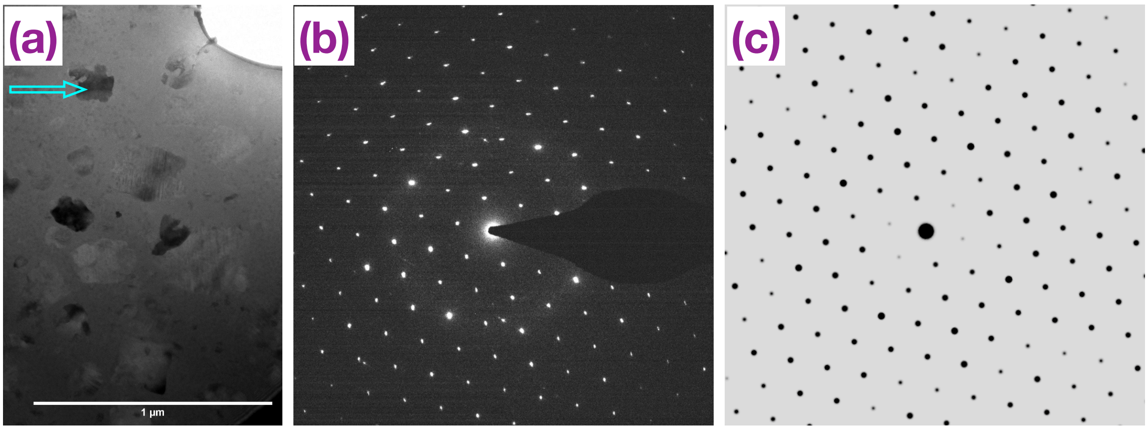

Figure 10. (a) TEM bright-field image of the specimen annealed at 475 °C for 34 min; (b) single-crystal-like SAED pattern taken from the grain pointed out in (a); (c) simulated electron diffraction pattern of $Cu_{10}Zr_7$ with the zone axis [0 1 1] (ICDD database PDF Card #01-082-3014).

To verify the $Cu_{10}(Zr,Hf)_7$ primary crystal phase identified from the XRD data analysis, more targeted SAED patterns were collected of single grains in the partially crystallized specimen by isolating the grains with a selected area aperture. Figure 10b shows an example of a single-crystal-like diffraction pattern taken from the grain marked in Figure 10a. The pattern is found to closely match the [0 1 1] zone axis pattern of $Cu_{10}Zr_7$ in the ICDD (International Centre for Diffraction Data [33]) database (PDF Card #01-082-3014) that is shown in Figure 10c. As mentioned earlier in Section 3.3, binary compounds $Cu_{10}Zr_7$ and $Cu_{10}Hf_7$ possess the same structure and similar lattice parameters, and hence this reference pattern is representative of $Cu_{10}(Zr,Hf)_7$ with random substitution of Zr and Hf on their sublattice. The close match between the measured and the reference electron diffraction patterns here provides additional support for the $Cu_{10}(Zr,Hf)_7$ as the primary crystal phase, affirming the earlier XRD analysis.

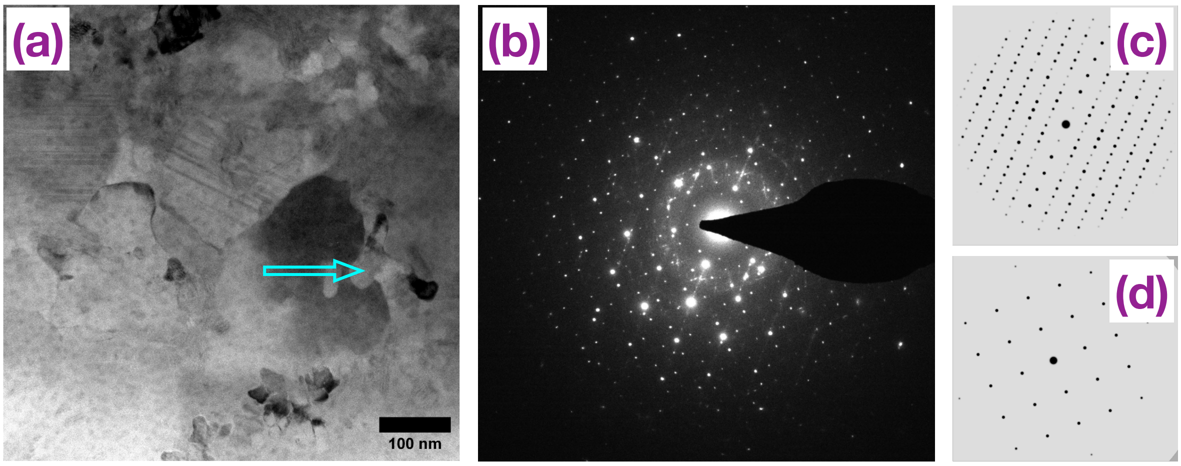

Figure 11. (a) TEM bright-field image of the specimen annealed at 475 °C for 65 min; (b) SAED pattern taken from the grain pointed out in (a); (c) simulated electron diffraction pattern of $Cu_{10}Zr_7$ with the zone axis [1 0 0] (ICDD database PDF Card #01-082-3014); (d) simulated electron diffraction pattern of $CuZr_2$ with the zone axis [0 0 1] (ICDD database PDF Card 04-002-0044).

The TEM image (Figure 9c) of the specimen annealed at 475 °C for 65 min shows the relatively bigger primary crystals together with finer microstructure in between them throughout the specimen, the latter attributable to the second crystallization event. The overall diffraction pattern comprises a high density of spots, some of which appear to have connected into a thin ring that is typical of a polycrystalline structure with random grain orientations. Selective diffraction targeting the finer microstructure between the primary crystals results in a complex moiré pattern due to double diffraction events involving two crystalline phases, as shown in Figure 11b (taken from the grain marked in Figure 11a). The pattern resembles a superimposition of the [1 0 0] pattern of $Cu_{10}Zr_7$ and the [0 0 1] pattern of the $CuZr_2$ (PDF Card 04-002-0044, same structure as $CuHf_2$) in the ICDD database, which are displayed in Figure 11c and 11d, respectively, with additional spots from the moiré. This affirms the conclusion from the XRD analysis that $Cu(Zr,Hf)_2$ is a new phase produced in the second crystallization event. The double diffraction with superimposed $Cu(Zr,Hf)_2$ and $Cu_{10}(Zr,Hf)_7$ patterns is believed to be caused by the technical difficulty in finding a single $Cu(Zr,Hf)_2$ grain that is not interrupted by primary $Cu_{10}(Zr,Hf)_7$ crystals upon diffraction, because the $Cu(Zr,Hf)_2$ grains are very small.

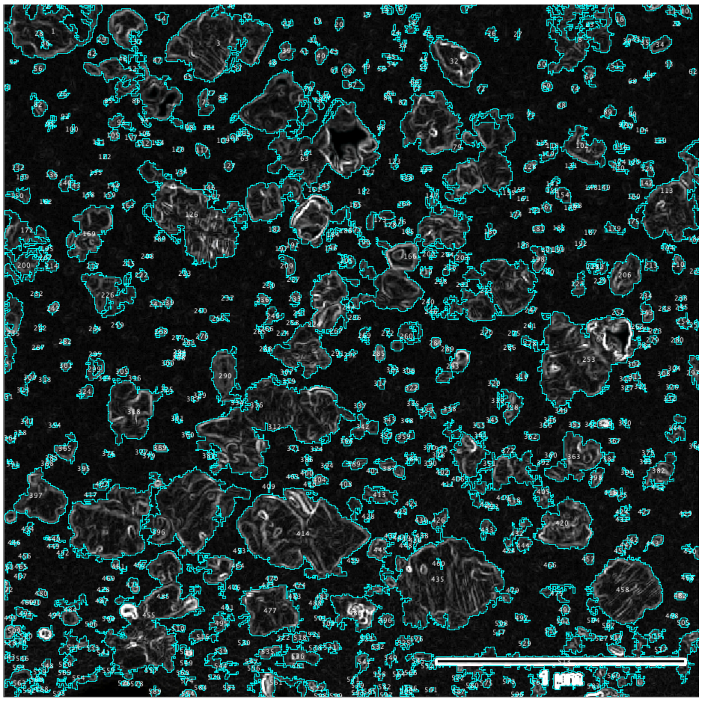

Figure 12. Particle (crystal grain) analysis for the TEM image (Figure 9b) of the specimen annealed at 475 °C for 34 min. The scale bar is 1 μm, same as in Figure 9b.

Finally, we make some broad estimates of number density and nucleation and growth rates of the primary crystals based on the TEM image (Figure 9b) of the specimen annealed at 475 °C for 34 min. The open-source program ImageJ [34] is used to perform particle (crystal grains, here) analysis on the TEM image. The identified grains are shown in Figure 12, the total number of which is 599. The areal fraction of the identified grains with respect to the entire image is 27%. According to the cumulative transformation curves in Figure 6, the transformed fraction corresponding to 34 min at 475 °C is 34%. These two fractions are in quite good agreement, especially if one considers the differences between the area-based statistics in the 2-D image analysis here and the heat-based (close to but not exactly the same as 3-D volume-based) statistics in the DSC data analysis.

The number density of the primary crystals is estimated to be 1.6×10^{21} m^{-3} using the total number of identified grains, the area of the image (2.75 × 2.75 μm) and the approximated thickness of the TEM foil in this region (50 nm). This number density is many orders of magnitude higher than the grain population (≈10^{12} to 10^{15} m^{-3}) in conventional metals/alloys typically with a tens-of-micron grain size. It comes as a result of the deeply supercooled state of the crystallizing liquid (here, glass heated above its glass transition temperature) which favors the nucleation of new nuclei over the growth of the existing ones.

Using the number density and the annealing time (deducting the ≈12 min incubation time revealed by DSC data analysis), the nucleation rate of the primary crystals is estimated to be 1.2×10^{18} m^{-3} s^{-1}. This is on the same order of magnitude as the maximum nucleation rate previously reported [35] for $Pd_{40}Cu_{30}Ni_{10}P_{20}$, another BMG with outstanding glass-forming ability which is based on the precious metal Pd. On the other hand, this nucleation rate is more than ten orders of magnitude higher than the maximum nucleation rate [35] in $Zr_{41.2}Ti_{13.8}Cu_{12.5}Ni_{10}Be_{22.5}$, yet another well-known BMG with outstanding glass-forming ability which contains substantial amount of toxic element Be.

To estimate the growth rate, the biggest primary crystals in the TEM image (Figure 9b) which have a diameter ≈500 nm are considered to have nucleated and started to grow at the end of the incubation time (12 min), and hence have grown over a time period of 22 min. This yields an approximate growth rate of 0.38 nm/s, which is extremely low.

It is noted that these estimates of crystal number density and nucleation and growth rates are only for 475 °C and an annealing time up to 34 min. Nevertheless, they do suggest that the high glass-forming ability of the $Cu_{46}Zr_{33.5}Hf_{13.5}Al_7$ BMG is mainly contributed by the slow crystal growth, similar to the case of $Pd_{40}Cu_{30}Ni_{10}P_{20}$. Meanwhile, the estimated high nucleation rate together with the low crystal growth rate implies a good opportunity to control the crystallization of the BMG towards glass-nanocrystal composite or fully nanocrystalline structure.

4. Conclusions

We have investigated the crystallization behavior of the newly discovered Cu-based $Cu_{46}Zr_{33.5}Hf_{13.5}Al_7$ BMG using DSC, XRD, and TEM. Our main conclusions are as follows:

- Isochronal DSC data reveal a high activation energy of ≈360 kJ/mole for crystallization, consistent with the high glass-forming ability of the alloy.
- Isothermal DSC data at seven different temperatures (470 to 500 °C) are all well fitted by the KJMA model that incorporates two crystallization events. The fitted model parameters including incubation times and Avrami exponents are reported. The Avrami exponent of the primary crystallization event increases from 4.4 at 470 °C to 6.4 at 500 °C for the primary crystallization, which is understood as resulting from non-steady state homogeneous nucleation and 3-D interface-controlled growth. The Avrami exponent of the second crystallization event stays relatively stable around 2.6 to 2.8 across the seven temperatures, which is attributed to primary-crystal-induced heterogeneous nucleation and an effectively sub-3-D growth mode. Cumulative transformation curves and corresponding TTT diagrams are obtained from the isothermal DSC data.
- XRD analysis of a partially crystallized and a fully crystallized specimen, both annealed at 475 °C in the calorimeter, identifies the orthorhombic $Cu_{10}(Zr,Hf)_7$ to be the primary crystal phase and the tetragonal $Cu(Zr,Hf)_2$ to be the new phase produced in the second crystallization event. The phase identities are further confirmed by TEM using selected area electron diffraction.
- Analysis of the TEM image of the partially crystallized specimen reveals a high number density on the order of 10^{21} m^{-3}, a high nucleation rate ≈10^{18} m^{-3} s^{-1}, and an extremely low growth rate ≈0.38 nm/s of the primary crystals. These data suggest that between the nucleation and growth rates, the latter makes greater contribution to the high glass-forming ability of this BMG. The high nucleation and low crystal growth rates imply that this BMG is particularly suitable to serve, through controlled devitrification, as a precursor to glass-nanocrystal composite or bulk nanocrystalline structures.

Author Contributions: Conceptualization, D.X.; methodology, D.X., M.K.S.; validation, formal analysis, and investigation, J.S.S., T.D.K., T.T., L.C., M.K.S., D.X.; resources, D.X., M.K.S.; writing—

original draft preparation, D.X.; funding acquisition, D.X., M.K.S. All authors have read and agreed to the published version of the manuscript.

Funding: This research was partially supported by the U.S. National Science Foundation under grants No. DMR 2221854 and DMR 1945520. The APC was waived by MDPI as this is an invited feature paper.

Data Availability Statement: The data that support the findings of this study are available from the corresponding author upon reasonable request.

Acknowledgments: TEM was performed at the Oregon State University Electron Microscope Facility which is supported by NSF MRI Grant No. 1040588, the Murdock Charitable Trust, and the Oregon Nanoscience and Micro-Technologies Institute.

Conflicts of Interest: The authors declare no conflict of interest.

References:

1. Johnson, W.L. Bulk glass-forming metallic alloys: Science and technology. *Mrs Bulletin* **1999**, *24*, 42-56, doi:10.1557/s0883769400053252.
2. Schroers, J. BULK Metallic Glasses. *Physics Today* **2013**, *66*, 32-37, doi:10.1063/pt.3.1885.
3. Loffler, J.F. Bulk metallic glasses. *Intermetallics* **2003**, *11*, 529-540, doi:10.1016/s0966-9795(03)00046-3.
4. Greer, A.L. METALLIC GLASSES. *Science* **1995**, *267*, 1947-1953, doi:10.1126/science.267.5206.1947.
5. Inoue, A. Stabilization of metallic supercooled liquid and bulk amorphous alloys. *Acta Materialia* **2000**, *48*, 279-306, doi:10.1016/s1359-6454(99)00300-6.
6. Schroers, J. The superplastic forming of bulk metallic glasses. *Jom* **2005**, *57*, 35-39, doi:10.1007/s11837-005-0093-2.
7. Schroers, J. Processing of Bulk Metallic Glass. *Advanced Materials* **2010**, *22*, 1566-1597, doi:10.1002/adma.200902776.
8. Johnson, W.L.; Na, J.H.; Demetriou, M.D. Quantifying the origin of metallic glass formation. *Nature Communications* **2016**, *7*, 10313, doi:10.1038/ncomms10313.
9. Choi-Yim, H.; Xu, D.H.; Johnson, W.L. Ni-based bulk metallic glass formation in the Ni-Nb-Sn and Ni-Nb-Sn-X (X = B,Fe,Cu) alloy systems. *Applied Physics Letters* **2003**, *82*, 1030-1032, doi:10.1063/1.1544434.
10. Kim, W.; Oh, H.S.; Park, E.S. Manipulation of thermal and mechanical stability by addition of multiple equiatomic rare-earth elements in Al-TM-RE metallic glasses. *Intermetallics* **2017**, *91*, 8-15, doi:10.1016/j.intermet.2017.07.019.
11. Xu, D.H.; Lohwongwatana, B.; Duan, G.; Johnson, W.L.; Garland, C. Bulk metallic glass formation in binary Cu-rich alloy series - Cu100-xZrx (x=34, 36 38.2, 40 at.%) and mechanical properties of bulk Cu64Zr36 glass. *Acta Materialia* **2004**, *52*, 2621-2624, doi:10.1016/j.actamat.2004.02.009.
12. Xu, D.H.; Duan, G.; Johnson, W.L.; Garland, C. Formation and properties of new Ni-based amorphous alloys with critical casting thickness up to 5 mm. *Acta Materialia* **2004**, *52*, 3493-3497, doi:10.1016/j.actamat.2004.04.001.
13. Xu, D.H.; Duan, G.; Johnson, W.L. Unusual glass-forming ability of bulk amorphous alloys based on ordinary metal copper. *Physical Review Letters* **2004**, *92*, 245504, doi:10.1103/PhysRevLett.92.245504.
14. Saini, J.S.; Palian, C.; Lei, F.Q.; Dyall, A.; AuYeung, N.; McQuade, R.; Gupta, S.K.; Cann, D.P.; Xu, D.H. Rare-earth and precious-metal free Cu-based metallic glasses with superior glass-forming ability and processability. *Applied Physics Letters* **2020**, *116*, 011901, doi:10.1063/1.5131645.
15. Saini, J.S.; Miska, J.P.; Lei, F.Q.; AuYeung, N.; Xu, D.H. Hafnium based metallic glasses with high density and high glass-forming ability. *Journal of Alloys and Compounds* **2021**, *882*, 160896.
16. Ponnambalam, V.; Poon, S.J.; Shiflet, G.J. Fe-based bulk metallic glasses with diameter thickness larger than one centimeter. *Journal of Materials Research* **2004**, *19*, 1320-1323, doi:10.1557/jmr.2004.0176.
17. Zhang, M.; Song, Y.; Lin, H.; Li, Z.; Li, W. A Brief Introduction on the Development of Ti-Based Metallic Glasses. *Frontiers in Materials* **2022**, *8*, 814629, doi:10.3389/fmats.2021.814629.
18. Sun, B.B.; Wang, Y.B.; Wen, J.; Yang, H.; Sui, M.L.; Wang, J.Q.; Ma, E. Artifacts induced in metallic glasses during TEM sample preparation. *Scripta Materialia* **2005**, *53*, 805-809, doi:10.1016/j.scriptamat.2005.06.007.
19. Blaine, R.L.; Kissinger, H.E. Homer Kissinger and the Kissinger equation. *Thermochimica Acta* **2012**, *540*, 1-6, doi:10.1016/j.tca.2012.04.008.
20. Liu, L.; Wu, Z.F.; Zhang, J. Crystallization kinetics of Zr55Cu30Al10Ni5 bulk amorphous alloy. *Journal of Alloys and Compounds* **2002**, *339*, 90-95, doi:10.1016/s0925-8388(01)01977-6.
21. Mitrovic, N.; Roth, S.; Eckert, J. Kinetics of the glass-transition and crystallization process of Fe72-xNbxAl5Ga2P11C6B4 (x=0,2) metallic glasses. *Applied Physics Letters* **2001**, *78*, 2145-2147, doi:10.1063/1.1361099.
22. Meng, C.F.; Chen, S.Y.; Qiao, M.Y.; Shao, Z.J. DETERMINATION OF ACTIVATION-ENERGY FOR CRYSTALLIZATION IN METALLIC-GLASS BY SMALL-ANGLE X-RAY-SCATTERING. *Journal of Non-Crystalline Solids* **1992**, *144*, 308-311, doi:10.1016/s0022-3093(05)80415-6.

23. Cai, A.H.; Ding, D.W.; An, W.K.; Zhou, G.J.; Luo, Y.; Li, J.H.; Peng, Y.Y. Effect of Ni substitution on glass forming ability, mechanical, electrical and thermal properties of Cu-Zr-Ti glass forming alloys. *Materials Chemistry and Physics* **2015**, *151*, 243-251, doi:10.1016/j.matchemphys.2014.11.060.
24. Park, S.O.; Lee, J.C.; Kim, Y.C.; Fleury, E.; Sung, D.S.; Kim, D.H. Crystallization kinetics of the CU43Zr43Al7Ag7 amorphous alloy. *Materials Science and Engineering a-Structural Materials Properties Microstructure and Processing* **2007**, *449*, 561-564, doi:10.1016/j.msea.2006.02.445.
25. Duan, G.; Xu, D.H.; Zhang, Q.; Zhang, G.Y.; Cagin, T.; Johnson, W.L.; Goddard, W.A. Molecular dynamics study of the binary Cu46Zr54 metallic glass motivated by experiments: Glass formation and atomic-level structure. *Physical Review B* **2005**, *71*, 224208, doi:10.1103/PhysRevB.71.224208.
26. Kelton, K.F.; Gangopadhyay, A.K.; Kim, T.H.; Lee, G.W. A case for local icosahedral order in undercooled metallic liquids and the influence on the nucleation barrier. *Journal of Non-Crystalline Solids* **2006**, *352*, 5318-5324, doi:10.1016/j.jnoncrysol.2006.08.009.
27. Xu, D.H.; Chen, F.Z. Continuously variable atomic structure in monatomic metallic glasses through active icosahedral dynamics below glass transition temperature. *Journal of Applied Physics* **2018**, *124*, 125101, doi:10.1063/1.5049448.
28. Xu, D.H.; Wang, Z.M.; Chang, T.Y.; Chen, F.Z. Inverted core-shell potential energy landscape of icosahedral clusters in deeply undercooled metallic liquids and glasses and its effect on the glass forming ability of bcc and fcc metals. *Journal of Physics-Condensed Matter* **2020**, *32*, 405402, doi:10.1088/1361-648X/ab9913.
29. Chang, T.Y.; Wang, Z.M.; Xu, D.H. Formation energetics/dynamics of icosahedral clusters in supercooled metallic liquids in the dynamic equilibrium regime: Gibbs free energy, entropy, enthalpy, and connection to coordination shells. *Journal of Materials Research*, **2023**, 38, 179–186, doi:10.1557/s43578-022-00664-5.
30. Chang, T.Y.; Wang, Z.M.; Xu, D.H. Icosahedral clusters in Cu100-xZrx (x=32,34,36,38.2,40 at.%) metallic glasses near the peak of glass-forming ability (x=36): A balance between population and encaging strength. *Journal of Physics and Chemistry of Solids* **2021**, *154*, 110076, doi:10.1016/j.jpcs.2021.110076.
31. Doebelin, N.; Kleeberg, R. Profex: a graphical user interface for the Rietveld refinement program BGMN. *Journal of Applied Crystallography* **2015**, *48*, 1573-1580, doi:10.1107/s1600576715014685.
32. Jain, A.; Ong, S.P.; Hautier, G.; Chen, W.; Richards, W.D.; Dacek, S.; Cholia, S.; Gunter, D.; Skinner, D.; Ceder, G.; et al. Commentary: The Materials Project: A materials genome approach to accelerating materials innovation. *Apl Materials* **2013**, *1*, 011002, doi:10.1063/1.4812323.
33. Gates-Rector, S.; Blanton, T. The Powder Diffraction File: a quality materials characterization database. *Powder Diffraction* **2019**, *34*, 352-360, doi:10.1017/s0885715619000812.
34. Schneider, C.A.; Rasband, W.S.; Eliceiri, K.W. NIH Image to ImageJ: 25 years of image analysis. *Nature Methods* **2012**, *9*, 671-675, doi:10.1038/nmeth.2089.
35. Xu, D.H.; Johnson, W.L. Crystallization kinetics and glass-forming ability of bulk metallic glasses Pd40Cu30Ni10P20 and Zr41.2Ti13.8Cu12.5Ni10Be22.5 from classical theory. *Physical Review B* **2006**, *74*, 024207, doi:10.1103/PhysRevB.74.024207.